Available online at www.sciencedirect.com

ScienceDirect

Ceramics International 39 (2013) 9421–9428

CERAMICS INTERNATIONAL

www.elsevier.com/locate/ceramint

# Effect of sintering atmosphere on densification, redox chemistry and conduction behavior of nanocrystalline Gd-doped $CeO_2$ electrolytes

Surendra Babu Anantharaman, Ranjit Bauri*

*Department of Metallurgical and Materials Engineering, Indian Institute of Technology Madras, Chennai 600036, India*

Received 12 April 2013; received in revised form 6 May 2013; accepted 7 May 2013
Available online 23 May 2013

**Abstract**

Nanocrystalline 10 mol% gadolinia doped ceria (GDC) was processed and sintered in air and oxygen to study the role of sintering atmosphere on densification and the redox reaction ($Ce^{4+}\leftrightarrow Ce^{3+}$) and its effect on the conduction behavior. The density of the air-sintered sample was higher than the oxygen-sintered sample. X-ray photoelectron spectroscopy (XPS) confirmed the presence of higher fraction of $Ce^{3+}$ and Raman spectroscopy revealed higher concentration of oxygen vacancies in GDC sintered in air indicating higher degree of reduction in air compared to oxygen atmosphere. Impedance spectroscopy studies revealed breaks in the slope of the Arrhenius plot of bulk conductivity indicating presence of different conduction mechanisms which can be related to the redox and defect chemistry. GDC sintered in oxygen atmosphere showed higher ionic conductivity and lower activation energy than the air sintered sample in lower temperatures whereas it showed higher activation energy in the higher temperature range owing to a change in the redox and defect chemistry.


*Keywords:* A. Sintering; B. Spectroscopy; C. Electrical conductivity; D. $CeO_2$

## 1. Introduction

Solid oxide fuel cell (SOFC) is a system which converts chemical energy to electrical energy at higher efficiency and without pollution. The high working temperature of SOFCs has been a major hurdle in the realization of this important green technology in real life. Therefore, intermediate temperature solid oxide fuel cells (IT-SOFC) are becoming imperative due to their ability to work at lower temperatures that help reducing the high temperature degradation and provide enhanced life time to cell components. However, this necessitates the development of electrolyte materials which can provide enough conductivity at such temperatures. Ceria based materials are promising candidates for IT-SOFC electrolytes due to their higher conductivity compared to conventional zirconia based electrolytes. However, pure ceria remains to be a poor ionic conductor. The conductivity can be enhanced by addition of dopants. When $CeO_2$ is doped aliovalently with a cation $Md^{(4-n)+}$, oxygen non-stoichiometry is introduced and oxygen vacancies are generated in the lattice which assist in conduction of oxygen ions and hence, enhance the conductivity [1,2]. For divalent dopants, $n$=2 and alkaline metals like $Ca^{2+}$, $Mg^{2+}$ fall into this category. The dopant in this case has an effective charge of −2 ($Md_{Ce}''$). The defect formation reaction is shown in Eq. (1). The coulombic interaction between oppositely charged dopants and oxygen vacancies form defect associates and the dissociation of the defect complex $(Md_{Ce}''V_o^{\cdot\cdot})^{\times}$ thus formed generates free oxygen vacancies (Eq. (2)).

$$MdO \overset{CeO_2}{\Longrightarrow} Md''_{Ce} + V_O^{\bullet\bullet} + O_O^{\times} \quad (1)$$

$$Md''_{Ce}V_o^{\bullet\bullet} \leftrightarrow Md''_{Ce} + V_o^{\bullet\bullet} \quad (2)$$

when the defects are fully associated, $(Md_{Ce}''V_o^{\cdot\cdot})^{\times} \gg [V_o^{\cdot\cdot}]$ and $(Md_{Ce}''V_o^{\cdot\cdot})^{\times} = C_{Ce}$ where, $C_{Ce}$ is the total dopant concentration in terms of site fraction of the cation site.

For trivalent dopants like $Sm^{3+}$, $Gd^{3+}$,$Y^{3+}$, $Nd^{3+}$, $n=1$ and the dopant has single negative effective charge ($Md_{Ce}'$). The defect complex in this case is $(Md_{Ce}'V_o^{\cdot\cdot})^{\bullet}$ which has single positive effective charge and forms through the reaction

$$Md'_{Ce} + V_o^{\bullet\bullet} \leftrightarrow (Md'_{Ce}V_o^{\bullet\bullet})^{\bullet} \quad (3)$$

*Corresponding author. Tel.: +91 44 22574778; fax: +91 44 22574752.
*E-mail addresses:* rbauri@iitm.ac.in, rbauri@gmail.com (R. Bauri).

0272-8842/$ - see front matter © 2013 Elsevier Ltd and Techna Group S.r.l. All rights reserved.
http://dx.doi.org/10.1016/j.ceramint.2013.05.059

An electrically neutral complex or the triplet $(Md_{Ce}'-V_o^{\cdot\cdot}-Md_{Ce}')^{\times}$ can also form as

$$2Md'_{Ce}+V_o^{\bullet\bullet}\leftrightarrow(Md'_{Ce}-V_o^{\bullet\bullet}-Md'_{Ce})^{\times} \quad (4)$$

This, however, needs cation diffusion which is difficult to occur. Therefore, reaction (3) is more likely to occur and hence, half of the trivalent dopant will be in association with oxygen vacancies and other half will be in isolated $Md_{Ce}'$ form [3].

$CeO_2$, doped or undoped, however, undergoes reduction from its $Ce^{4+}$ state to $Ce^{3+}$ state at low partial pressures of oxygen. Hence, the partial pressure of oxygen in the sintering atmosphere will have a bearing on this redox reaction which in turn can affect the densification and conduction behavior. The aim of the present investigation is precisely to understand this effect by XPS, Raman and impedance spectroscopy. An account of the conduction mechanism and its correlation with the redox chemistry has also been provided.

## 2. Experimental procedure

10 mol% $Gd_2O_3$ doped $CeO_2$ (GDC) was synthesized using solution combustion route. Stoichiometric amounts of Cerium nitrate ($Ce(NO_3)_3\cdot 6.5H_2O$, Alfa Aesar) and Gadolinium nitrate ($Gd(NO_3)_3\cdot 6.03H_2O$, Alfa Aesar) were mixed in a silica basin and citric acid monohydrate ($C_6H_8O_7\cdot H_2O$) was added as the fuel in stoichiometric ratio so that the sum of oxidizing and reducing valencies is zero as per the propellant chemistry concept [4–7]. Twenty five weight percent of polyethelyeneglycol (PEG) was added as a dispersant to the precursor salts and deionised water was added to produce a 0.1 M solution. The solution was first heated on a hot plate at around 250 °C and after gelation, the silica basin was covered with a stainless steel mesh and transferred into a preheated furnace at 600 °C. Combustion reaction was initiated and foamy powders were obtained in the silica basin. The powders were crushed in an agate mortar pestle and calcined at 800 °C for 1 h to remove the carbonaceous content. The calcined powders were subsequently ball-milled at 300 rpm in terpineol medium for 4 h to break the hard agglomerates. The milled powders were dried in an oven at 150 °C for 24 h. Powders were consolidated in to compacts in a 12 mm diameter die with a compaction pressure of 750 MPa. The green compacts were sintered at 1300 °C for 4 h in air and oxygen atmosphere separately. The flow rate of oxygen was maintained at 1.5 l/min. The compacts sintered in air and oxygen atmosphere are denoted as GDC-A and GDC-O respectively. The density of the sintered compacts was determined by Archimedes' principle.

The powder morphology was studied by scanning and transmission electron microscopy (SEM and TEM). Phase analysis was carried out by X-ray diffraction (XRD) on as-prepared and calcined powders and sintered compacts in a Bruker AXS diffractometer using Cu $K_\alpha$ radiation ($\lambda$=0.154 nm). Raman spectra of ball-milled powder and sintered compacts of GDC-A and GDC-O were collected using a Horiba Jobin Yuvon HR 800 UV-Raman spectrophotometer with an excitation wavelength of 632.8 nm. XPS studies were carried out on acetone cleaned sintered compacts using ESCA probe TPD system in ultra-high vacuum. Monochromatic source of Al $K_\alpha$ radiation with binding energy up to 1486.7 eV was chosen as incident radiation. $Ar^+$ sputtering on the sintered compacts was done to clean the surface and survey scan of 0–1200 eV was executed. Binding energies were calibrated with carbon 1 s peak position at 284.6 eV.

The electrical conductivity of the sintered compacts were measured using two-probe AC impedance on a Solartron 1260 impedance analyzer between 400 °C to 750 °C. Silver wires were used as current collectors and silver paste was applied on both sides of the sintered compacts for electrical contact. A frequency range of 1 MHz–0.1 Hz with an oscillation voltage of 100 mV was used for the measurements. The diameter and thickness of each sample was measured carefully before the measurements.

## 3. Results and discussion

### 3.1. Powder synthesis

According to thermo-chemical concepts of propellant chemistry, the sum of the oxidizing and reducing valencies in a redox mixture is zero [4]. The general combustion products are $CO_2$, $H_2O$ and $N_2$. Hence, C and H are the reducing elements and have positive valency of +4 and +1 respectively and oxidizing elements like O has negative valency of −2 and it is zero for nitrogen as it does not take part in the reaction. The equivalent valencies of the precursor compounds are calculated using these values.

The molar ratio of Gd to Ce in 10 mol% GDC is 0.18:0.82 and hence, the stoichiometric molar fraction of the fuel required to synthesize 10GDC is 0.83 and the reaction is as follows.

$$0.82Ce(NO_3)_3\,6.5H_2O+0.18Gd(NO_3)_3\,6.03H_2O+0.83C_6H_8O_7\,H_2O\rightarrow Ce_{0.82}Gd_{0.18}O_{1.91}+5CO_2+1.5N_2+11H_2O \quad (5)$$

The processed powder was foamy in appearance and was highly nanocrystalline as found by XRD, SEM and TEM analysis.

### 3.2. X-ray diffraction analysis

Fig. 1 shows the XRD patterns of the calcined powders and sintered compacts of GDC. The cubic fluorite phase of ceria was found in the calcined and ball-milled powders and no other undesirable phase was detected upon sintering. The crystallite size was calculated from the (111) peak using Scherrer's formula. The instrumental broadening was corrected using well annealed coarse grained alumina powder. The crystallite sizes are indicated on the respective XRD plots in Fig. 1. The as-prepared powder was very fine (8 nm) and growth took place on heating during calcinations and sintering leading to increase in the size.

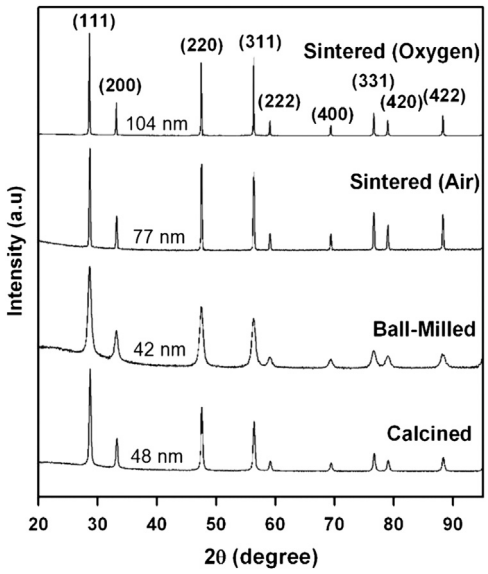


Fig. 1. XRD patterns of GDC powders and sintered pellets. The crystallite sizes in different conditions are shown on the respective plots.

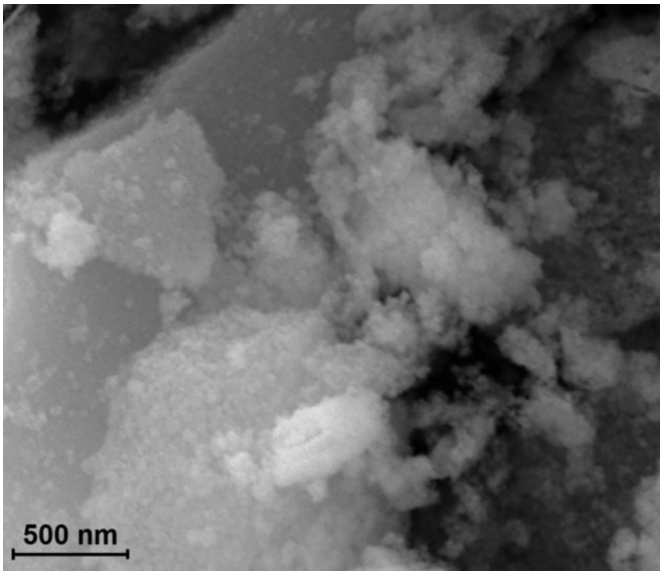


Fig. 2. SEM micrograph of the GDC powder.

### 3.3. Microstructure and density

The size and morphology of the powder was analyzed by SEM and TEM. The SEM micrograph in Fig. 2 shows ultra fine particles in the as processed powder. The bright field TEM image in Fig. 3 clearly reveals the equiaxed morphology of the powder. The size calculated from the TEM analysis matched well with that obtained from XRD.

The processed powder was sintered in two different atmospheres, namely air and oxygen. A sintered density of 94% of the theoretical density was obtained in air atmosphere without any sintering aid or sintering pressure. It should be noted that the sintering temperature and time used here was much lower

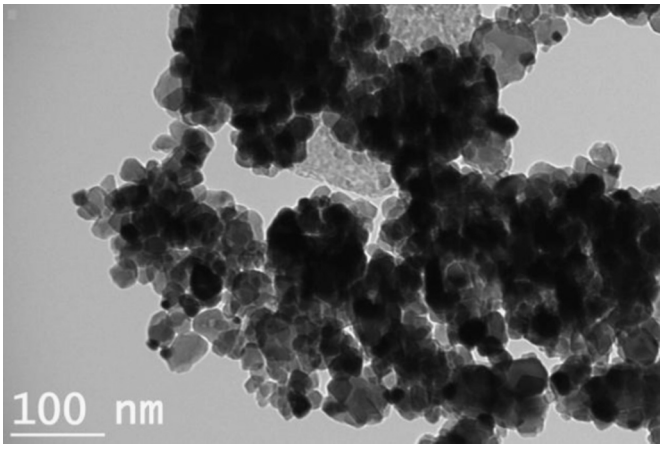


Fig. 3. TEM bright field image showing the morphology of the powder.

compared to those used for microcrystalline powders (e.g. 1500 °C for 10 h). As the driving force for the sintering process comes from the surface energy, this can be attributed to high surface area of the nanocrystalline powder. Ballmilling also helped in this respect by deagglomerating the powder resulting in high surface area. The shorter diffusion distance in the ultrafine powders also aids the sintering process.

The density, however, reduced from 94% to 90% in the oxygen sintered sample. This can be attributed to vacancy concentration related to the redox reaction ($Ce^{4+} \leftrightarrow Ce^{3+}$) in ceria. It is well known that $Ce^{4+}$ state in $CeO_2$ gets reduced to $Ce^{3+}$ at low oxygen partial pressures. The redox reaction in ceria can be written in the Kröger–Vink notation as

$$O_O^{\times} \leftrightarrow \frac{1}{2}O_2 + V_O^{\bullet\bullet} + 2e' \tag{6}$$

where, $V_o^{\cdot\cdot}$ is the oxygen vacancy created due to release of oxygen that leaves behind two electrons ($2e'$) which were provided by Ce to the oxygen $2p$ band [8]. The balance between oxygen vacancies and these electrons also maintain the charge neutrality in the lattice. The nonstoichiometry in $CeO_2$ is size dependent. It has been reported that it is easier to reduce nanocrystalline $CeO_2$ compared to its microcrystalline or single crystal counter parts as the grain boundaries present in large number in the ultrafine-grained material act as sites for the reduction on an atomic scale [9,10]. Therefore, the reduction in the present study can occur in air ($O_2$ partial pressure≈0.21 atm) due to the ultra fine size of the processed powder. The oxygen vacancies ($V_o^{\cdot\cdot}$) generated due to the reduction increase the vacancy concentration in the lattice. The higher vacancy concentration enhances the sintering process [11,12] as the vacancies facilitate the diffusion of Ce cations through the lattice [13]. Since oxygen gas evolves in the reduction reaction (reaction (6)), the reaction will move towards the left hand side according to the Le Chatelier principle if excess oxygen is present in the reaction chamber (oxygen sintering atmosphere) and hence, will reduce the extent of ceria reduction. Therefore, the oxygen vacancy concentration is expected to be lower in the oxygen sintered sample compared to the air sintered sample and hence, the

decrease in the sintered density. This was established by Raman and XPS studies as described below.

### 3.4. Raman spectroscopy

The Raman spectra of ball milled and sintered samples exhibit three bands as shown in Fig. 4(a). Stokes vibrational $F_{2g}$ mode observed at 464 $cm^{-1}$ corresponds to cubic fluorite structure of $CeO_2$. Peaks observed at 550 $cm^{-1}$ and 600 $cm^{-1}$ correspond to intrinsic and extrinsic (due to aliovalent doping) oxygen vacancies respectively [14–16]. A Lorentzian peak profile was used to fit all the peaks. It can be seen that the $F_{2g}$ peak at 464 $cm^{-1}$ shifted toward lower energy in the ball-milled condition. This shift in the Raman peak of ceria has been attributed to combined effects of phonon confinement due to nano size effect and lattice strain associated with defect species [14,17]. The peak shifted toward higher energy and almost coincided with 464 $cm^{-1}$ after sintering. This can be attributed to reduced nano size effect as the crystals grow on heating and migration of oxygen vacancies toward the surface at higher temperature that promotes improved phonon lifetime [14]. The oxygen vacancy concentration was determined from the area ratio of the peaks at 550 $cm^{-1}$ and 464 $cm^{-1}$ ($A_{550}/A_{464}$) [15,16] and plotted in Fig. 4(b). The oxygen vacancy peaks were deconvoluted for this purpose as shown in the inset of Fig. 4(b). It was observed that while the concentration of oxygen vacancies remained almost unchanged in the oxygen sintered sample the same was much higher in compacts sintered in air (0.044) compared to the ball milled powder (0.021). This indicates that reduction of ceria occurs during sintering in air atmosphere producing oxygen vacancies (reaction (6)) while the extent of reduction is much lower in oxygen atmosphere. This is further corroborated by the XPS data.

### 3.5. X-ray photoelectron spectroscopy

XPS studies were performed to examine the oxidation state of cerium in the sintered compacts. The peaks observed at 141.6 eV and 146.8 eV at the lower energy side of the spectrum (Fig. 5a) represent the Ce $4d_{3/2}$ and Ce $4d_{5/2}$ spin-orbit spilitting respectively with carbon 1s peak being calibrated to 284.6 eV [18]. The O 1s peak at around 530 eV belongs to lattice oxygen. $CeO_2$ ($Ce^{4+}$) exhibits three pairs of

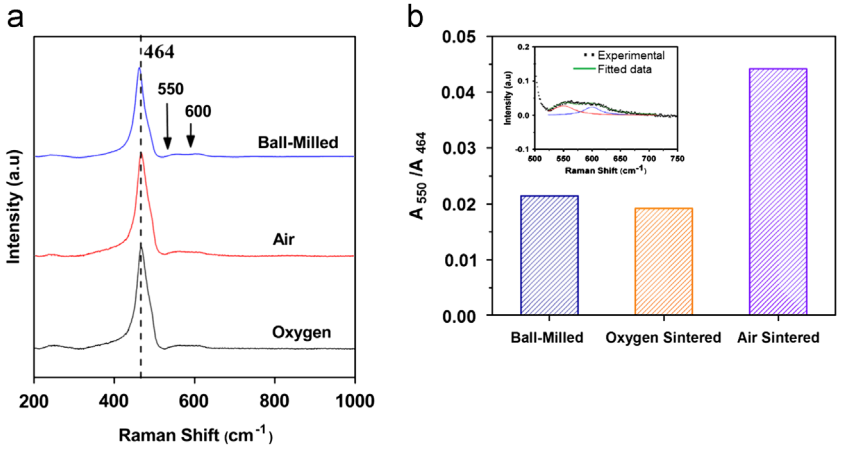


Fig. 4. (a) Raman spectra of ball-milled powder and sintered pellets. (b) Oxygen vacancy concentration. The deconvoluted oxygen vacancy peaks are shown in (b).

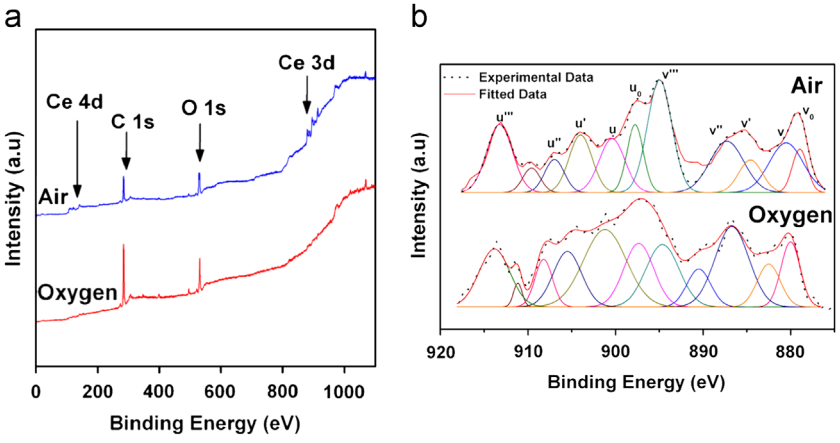


Fig. 5. (a) XPS spectra of GDC sintered in air and oxygen atmosphere. (b) Ce 3d spectrum of GDC-A and GDC-O.

spin-orbit doublets or six peaks corresponding to Ce 3d photoemissions. The multiple states are the result of different Ce 4f level occupencies in the final state. The higher energy pair, for example, correspond to the Ce $3d^9$ O $2p^6$ Ce $4f^0$ final state. The other four peaks arise from a mixture of Ce $3d^9$ O $2p^5$ Ce $4f^1$ and Ce $3d^9$ O $2p^4$ Ce $4f^2$ [19]. The Ce 3d spectrum of $Ce^{3+}$, on the other hand, shows two pairs of doublets due to the absence of Ce 4f $^0$ states. A partially reduced $CeO_2$ will thus have a mixture of these two Ce 3d spectra [14,20,21]. In the present case, the Ce 3d spectrum was deconvoluted to clearly identify the peak positions (Fig. 5b). It can be seen that apart from the Ce 3d doublets corresponding to $Ce^{4+}$ states ($v$, $v''$,$v'''$, $u$, $u''$, $u'''$) the XPS spectra of the sintered pellets also show presence of additional peaks ($v_o$, $v'$, $u_o$, $u'$) which correspond to $Ce^{3+}$ states indicating partial transformation of $Ce^{4+}$ to $Ce^{3+}$. The fraction of $Ce^{3+}$ was determined by finding the integrated peak areas corresponding $Ce^{3+}$ and $Ce^{4+}$ states and taking the ratio of the $Ce^{3+}$ to the total ($Ce^{4+}$+$Ce^{3+}$) area [14,21]. It was found that fraction of $Ce^{3+}$ was higher in the air sintered sample (~39%) compared to the oxygen sintered sample (~21%). Though these are approximate values and some level of error is always involved in such calculations due to the complexity of the mixed spectrum, however, the important point to be noted here is that it is in the same ratio (~2:1) as the ratio of oxygen vacancy concentrations in the air and oxygen sintered samples (Fig. 4b). This confirms that the extent of ceria reduction is less in oxygen atmosphere. The density reduction from 94% to 90% in the GDC-O sample is thus corroborated by the Raman and XPS data.

### 3.6. Electrical conductivity

Impedance spectroscopy was used to measure the electrical conductivity of GDC-A and GDC-O samples between 400 and 750 °C. The Nyquist plots are shown in Fig. 6. Grain (or bulk) and grain boundary contributions to conductivity were calculated from the real intercept based on the frequency dispersion as shown in Fig. 6(a) (the numbers indicated are log of frequency). The conductivity was calculated from the intercept on the real axis ($R$) and the dimensions of the sample (thickness, $l$ and area, $A$) using the formula $\sigma = l/RA$. Two differences should be noted here between the oxygen and air sintered samples. First, the final dimensions of the two samples were not exactly the same. The diameter and thickness of the air sintered sample was 10.8 mm and 1.1 mm respectively whereas these were 11 mm and 1.38 mm respectively for the oxygen sintered sample. This, however, is not an issue as the geometric factor (A/$l$) takes care of it. Secondly, the grain and grain boundary contributions could be easily resolved only up to 700 °C in case of the air sintered sample whereas it was possible to separate the two contributions beyond 700 °C in the oxygen sintered sample.

The temperature dependence of ionic conductivity follows an Arrhenius type relation

$$\sigma = \frac{\sigma_0}{T}\exp\left(\frac{-E_a}{k_B T}\right) \tag{7}$$

here, $\sigma_o$ is the pre-exponential factor, $E_a$ is the activation energy, $T$ is the absolute temperature and $k_B$ is Boltzmann's constant. The activation energy is obtained from the slope of the log scale plot (Arrhenius plot) of the equation. The Arrhenius plots for grain, grain boundary and total conductivity for GDC-A and GDC-O samples were obtained from the conductivity data.

#### 3.6.1. Grain conductivity

The Arrhenius plot for grain conductivity is shown in Fig. 7 (a). It can be seen that there is a break in the slope resulting in two different activation energies in the lower and higher temperature regions. The jump in the slope at higher temperature seems to be induced by a change in the intermediate temperature zone as can be seen from Fig. 7(a). This can be correlated with the defect and redox chemistry that play a major role on the ionic conduction. In an ionic conductor, different temperature zones of conductivity can be found based on the interaction between defect species and their thermodynamics [22,23]. At lower temperature the concentration of charge carrying defects is dictated by the coulombic interaction and thermodynamic equilibrium between oppositely charged defect species. At the intermediate temperature range the conductivity is determined by the charge carrying defects population which is controlled by a dopant or impurity and the

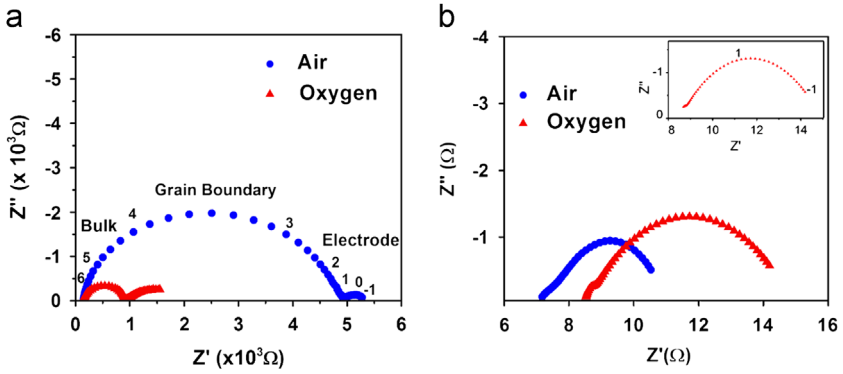


Fig. 6. Nyquist plots at (a) 400 °C and (b) 700 °C. The inset of (b) shows the half-tear drop shaped low frequency arc. Numbers on the plots are log of frequency (Hz).

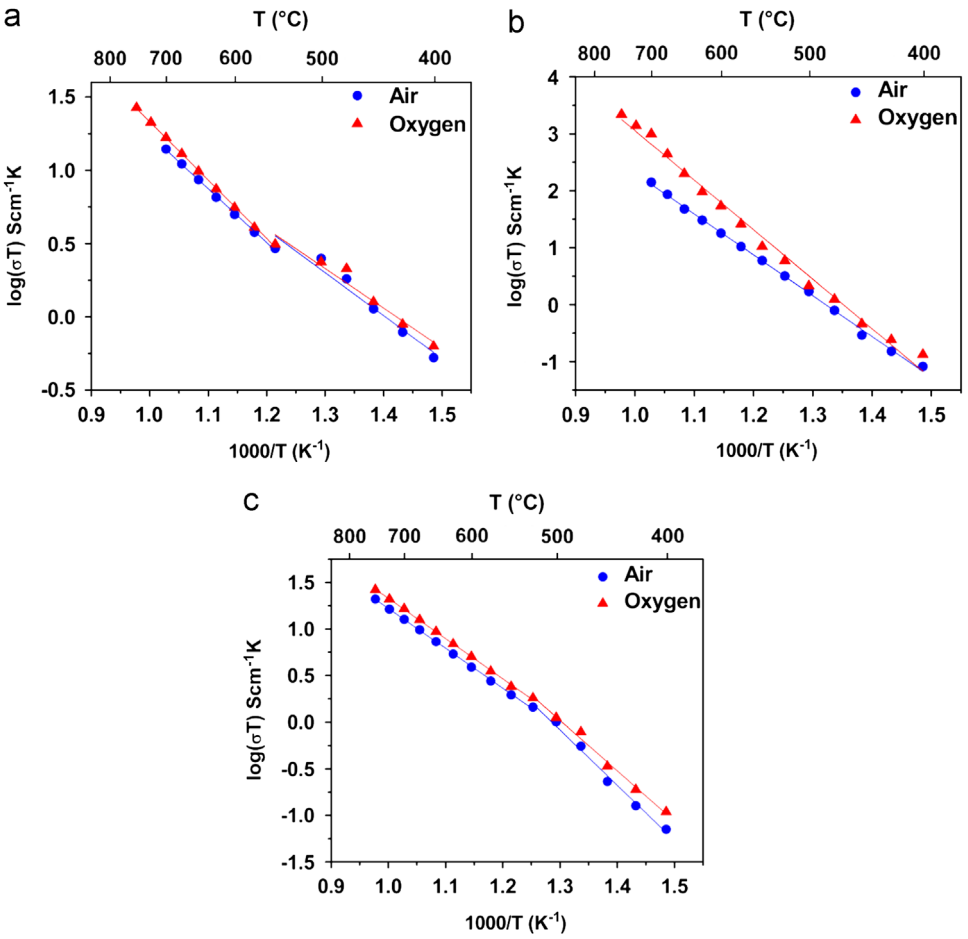


Fig. 7. Arrhenius plots of (a) bulk (grain) conductivity, (b) grain boundary conductivity and (c) total conductivity.

high temperature region is dominated by intrinsic defects [22,23]. The redox reaction in ceria (Eq. (6)) generates electrons which are localized in Ce sites ($2Ce'_{Ce}$) as it is energetically more favorable to form an oxygen vacancy near a pair of Ce atoms [8]. This defect along with the resulting distortion is known as polaron. Thus, in partially reduced ceria the different regions described above can be related to these three defect species, namely oxygen vacancies, polarons and dopants. The observed break also agrees well with some recent literature reports [24,25] on partially reduced ceria. The activation energy for grain conductivity in the GDC-O and GDC-A samples were found to be 0.54 eV and 0.57 eV respectively in the lower temperature region. These values are closer to activation energy for oxygen ion conduction in $CeO_2$ lattice [26]. It can be thus said that the lower temperature region is the ionic conduction region which is dictated by interaction between oxygen vacancies and the dopant ions. The ionic conductivity of the GDC-O sample was higher than the GDC-A samples as is also obvious from smaller semicircles in Fig. 6(a). For example, the grain conductivity values at 475 °C are $24.3 \times 10^{-4}$ and $27.3 \times 10^{-4}$ S cm$^{-1}$ for GDC-A and GDC-O samples respectively. This can be attributed to the extent of reduction of ceria in air and oxygen atmospheres. As shown conclusively by the Raman and XPS data above, the extent of reduction is higher in air sintering. The higher vacancy concentration due to greater reduction increases the likelihood of formation of defect associates like $(Gd_{Ce}{}'V_O^{\bullet\bullet})^{\bullet}$ which restricts oxygen vacancy migration [23] leading to lower ionic conductivity and higher activation energy in the GDC-A sample.

The slope changes toward higher activation energy in the high temperature region. This can be related to the redox reaction occurring in the ceria lattice. The electrons generated due to the reduction reaction (Eq. 6) are localized on Ce sites ($2Ce'_{Ce}$) and this defect is known as small polaron. It has been established that the *n*-type conductivity in reduced $CeO_2$ is due to hopping motion of the small polaron from one Ce site to the adjacent one [27,28]. The motion of the polarons is thermally activated i.e. they need thermal energy for the hopping motion and hence, are expected to be more prevalent at higher temperature. The ceria samples can also undergo reduction while being heated up to higher temperature during conductivity measurement. Therefore, the $CeO_2$ lattice contains two types of charge carrying species namely, oxygen vacancies and polarons, in the higher temperature region and gives rise to mixed ionic and electronic conductivity (MIEC). A typical nature of the Nyquist plot from a mixed ionic-electronic conductor is the presence of a low-frequency half-tear drop shaped arc [29,30]. The impedance plot of GDC-A and GDC-O samples did exhibit a half-tear drop shaped spectrum at low

frequencies at high temperatures as shown clearly in the inset of Fig. 6(b). The activation energy of the GDC-O samples was found to be higher (0.79 eV) compared to GDC-A sample (0.73 eV) in the mixed conducting region. This can be again attributed to the extent of redox reaction and the reduction of ceria during the thermal exposure in the conductivity measurement. Due to lesser extent of reduction in oxygen atmosphere sintering the concentration of $Ce^{3+}$ is lower in the GDC-O sample in the beginning of conductivity measurement. This will facilitate the redox reaction, $Ce^{4+}\leftrightarrow Ce^{3+}$ (due to less concentration of the product, $Ce^{3+}$), during heating the sample for conductivity measurement and hence, will generate more $Ce^{3+}$ with increasing temperature in the GDC-O sample compared to the GDC-A sample. This will result in increase in the jump distance of the charge carriers due to lattice expansion as the size of $Ce^{3+}$ ions (114.3 pm) is bigger than $Ce^{4+}$ ions (97 pm) [31]. Consequently the activation energy for conduction increases in the GDC-O sample.

### 3.6.2. Grain boundary conductivity

Fig. 7(b) shows the Arrhenius plot for grain boundary conductivity for GDC-A and GDC-O samples. The grain boundary conductivities of GDC-A and GDC-O samples are comparable in the lower temperature region. However, it is higher for the GDC-O sample at higher temperature and the difference increases with increasing temperature as shown in Fig. 7(b). This can also be correlated with the redox reaction occurring in $CeO_2$. The conduction through grain boundaries in reduced ceria is predominantly controlled through space-charge layer (SCL) which in turn depends on the redox chemistry. As explained above, the reduction happens in larger extent in the GDC-O sample during conductivity measurement at higher temperature. The generation of vacancies due to the reduction and their greater mobility due to breaking of the defect associates at higher temperatures provides enhanced conduction paths through the SCL. The fine size of the material also helps in lowering the space charge potential [32,33] and building up the oxygen vacancy concentration near the grain boundaries owing to the shorter diffusion distance of vacancies toward the grain boundaries from grain interiors. This again enhances the conduction through grain boundaries at higher temperature.

The total conductivity, $\sigma_T$, was calculated from bulk and grain boundary conductivities ($1/\sigma_T=1/\sigma_g+1/\sigma_{gb}$) [34] and is plotted in Fig. 7(c). The trend in the total conductivity is controlled by the pattern of the individual contributions of grain and grain boundaries with respect to temperature. The total conductivity also shows break in the activation energy. However, the trend is reverse in this case as compared to the bulk conductivity. The activation energy values for total conductivity were found to be 1.17 and 1.07 eV at lower temperatures and 0.85 and 0.86 eV at higher temperatures for air and oxygen sintered samples respectively. This can be attributed to contribution from grain boundaries which are much less conductive at lower temperatures.

## 4. Conclusions

GDC synthesized using citrate–nitrate solution combustion route was highly nanocrystalline in nature with the cubic fluorite phase. The effect of sintering atmosphere on densification and defect chemistry was studied by XPS and Raman spectroscopy. The conduction behavior was studied using impedance spectroscopy. Following conclusions can be drawn from this study.

The density of air sintered (GDC-A) sample was higher than the oxygen sintered sample (GDC-O) owing to higher vacancy concentration that aids achieving better densification. The Arrhenius plot of bulk conductivity exhibited break in the slope which can be correlated with the redox and defect chemistry. The conduction mode changes from ionic at lower temperatures to mixed ionic-electronic at higher temperature due to introduction and hopping of the polarons as a result of reduction of ceria. The GDC-O sample showed higher ionic conductivity and lower activation energy in the lower temperature range while the activation energy of GDC-O was higher than the GDC-A sample in the mixed conduction range. The grain boundary conductivity, on the other hand, was similar at lower temperature and increased more rapidly at higher temperatures in the GDC-O sample compared to the GDC-A sample.

## Acknowledgment

We gratefully acknowledge the financial support received from Department of Science and Technology (DST), Government of India, for carrying out many studies in this research work.

## References

[1] H.L. Tuller, A.S. Nowick, Doped ceria as solid oxide electrolyte, Journal of the Electrochemical Society 122 (1975) 255–259.
[2] R.N. Blumenthal, F.S. Brugner, J.E. Garnier, The Electrical conductivity of CaO-doped nonstoichiometric cerium dioxide from 700 °C to 1500 °C, Journal of The Electrochemical Society 120 (1973) 1230–1237.
[3] J.A. Kilner, R.J. Brook, A study of oxygen ion conductivity in doped non-stoichiometric oxides, Solid State Ionics 6 (1982) 237–252.
[4] S.R. Jain, K.C. Adiga, V.R. Pai Verneker, A new approach to thermochemical calculations of condensed fuel-oxidiser mixtures, Combustion and Flame 40 (1981) 71–79.
[5] V. Vijaya Lakshmi, R. Bauri, A.S. Gandhi, S. Paul, Synthesis and characterization of nanocrystalline ScSZ electrolyte for SOFCs, International Journal of Hydrogen Energy 36 (2011) 14936–14942.
[6] D.A. Fumo, M.R. Morelli, A.M. Segadães, Combustion synthesis of calcium aluminates, Materials Research Bulletin 31 (1996) 1243–1255.
[7] A. Ringuede, J.A. Labrincha, J.R. Frade, A combustion synthesis method to obtain alternative cermet materials for SOFC anodes, Solid State Ionics 141–142 (2001) 549–557.
[8] N.V. Skorodumova, S.I. Simak, B.I. Lundqvist, I.A. Abrikosov, B. Johansson, Quantum origin of the oxygen storage capability of ceria, Physical Review Letters 89 (2002) 166601-1–166601-4.
[9] Y.M. Chiang, E.B. Lavik, I. Kosacki, H.L. Tuller, J.Y. Ying, Non-stoichiometry and electrical conductivity of nanocrystalline $CeO_{2-x}$, Journal of Electroceramics 1 (1997) 7–14.

[10] Y.M. Chiang, E.B. Lavik, I. Kosacki, H.L. Tuller, J.Y. Ying, Defects and transport properties of nanocrystalline $CeO_{2-x}$, Applied Physics Letters 69 (1997) 185–187.
[11] Z. He, H. Yuan, J.A. Glassrock, C. Chatzichristodoulou, J.W. Phair, A. Kaiser, S. Ramousse, Densification and grain growth during early-stage sintering of $Ce_{0.9}Gd_{0.1}O_{1.95-\delta}$ in a reducing atmosphere, Acta Materialia 58 (2010) 3860–3866.
[12] M. Ozawa, Effect of oxygen release on the sintering of fine $CeO_2$ powder at low temperature, Scripta Materialia 50 (2004) 61–64.
[13] P.L. Chen, I.W. Chen, Role of defect interaction in boundary mobility and cation diffusivity of $CeO_2$, Journal of the American Ceramic Society 77 (1994) 2289–2297.
[14] A. Kumar, S. Babu, A.S. Karakoti, A. Schulte, S. Seal, Luminescence properties of europium-doped cerium oxide nanoparticles: role of vacancy and oxidation states, Langmuir 25 (2009) 10998–11007.
[15] S.P. Li, J.Q. Lu, P. Fang, M.F. Luo, Effect of oxygen vacancies on electrical properties of $Ce_{0.8}Sm_{0.1}Nd_{0.1}O_{2-\delta}$ electrolyte: an in situ Raman spectroscopic study, Journal of Power Sources 193 (2009) 93–98.
[16] Z.Y. Pu, J.Q. Lu, M.F. Luo, Y.L. Xie, Study of oxygen vacancies in $Ce_{0.9}Pr_{0.1}O_{2-\delta}$ solid solution by in-situ X-ray diffraction and in situ Raman spectroscopy, Journal of Physical Chemistry C 111 (2007) 18695–18702.
[17] J.E. Spanier, R.D. Robinson, F. Zhang, S-W. Chan, I.P. Herman, Size-dependent properties of $CeO_{2-y}$ nanoparticles as studied by Raman scattering, Physical Review B 64 (2001) 245407-1-245407-8.
[18] J.F. Moulder, W.F. Stickle, P.E. Sobol, K.D. Bomben, Handbook of X-ray Photoelectron Spectroscopy, Perkin-Elmer Corporation, Minnesota, 1992.
[19] D.R. Mullins, S.H. Overbury, D.R. Huntley, Electronspectroscopy of single crystal and polycrystalline cerium oxide surfaces, Surface Science 409 (1998) 307–319.
[20] W. Xiao, Q. Guo, E.G. Wang, Transformation of $CeO_2$ (111) to $Ce_2O_3$ (0001), Chemical Physics Letters 368 (2003) 527–531.
[21] T. Ghosal, P.G. Fleming, J.D. Holmes, M.A. Morris, The stability of $Ce_2O_3$ nanodots in ambient conditions: a study using block copolymer templated structures, Journal of Materials Chemistry 22 (2012) 22949–22957.
[22] A.S. Nowick, D.S. Park, Fluorite type oxygen conductors, in: G. D. Mahan, W.L. Roth (Eds.), Superionic Conductors, Plenum Press, New York, 1976, pp. 395–412.
[23] J.A. Kilner, C.D. Waters, The effects of dopant cation-oxygen vacancy complexes on the anion transport properties of non-stoichiometric fluorite oxides, Solid State Ionics 6 (1982) 253–259.
[24] M. Hartmanova, M. Jergel, I. Thurzo, F. Kundracik, K. Gmucova, S. Chromik, L. Ortega, Thin film electrolytes: yttria stabilized zirconia and ceria, Russian Journal of Electrochemistry 39 (2003) 478–486.
[25] A.K. Baral, Ionic transport properties and their variations with grain size in nanostructured double doped cerias as $Ce_{0.8}Gd_{0.1}Pr_{0.1}O_{2-\delta}$ and $Ce_{0.8}Gd_{0.15}Pr_{0.05}O_{2-\delta}$, Electrochimica Acta 56 (2010) 667–675.
[26] R. Maric, S. Seward, P.W. Faguy, M. Oljaca, Electrolyte materials for intermediate temperature fuel cells produced via combustion chemical vapor condensation, Electrochemical and Solid State Letters 6 (2003) A91–A95.
[27] Y. Zhou, M.N. Rahaman, Effect of redox reaction on the sintering behavior of cerium oxide, Acta Materialia 45 (1997) 3635–3639.
[28] H.L. Tuller, A.S. Nowick, Small polaron electron transport in reduced $CeO_2$ single crystals, Journal of Physics and Chemistry of Solids 38 (1977) 859–867.
[29] W. Lai, S.M. Haile, Impedance spectroscopy as a tool for chemical and electrochemical analysis of mixed conductors: a case study of ceria, Journal of the American Ceramic Society 88 (2005) 2979–2997.
[30] J. Jamnick, J. Maier, Treatment of the impedance of mixed conductors equivalent circuit model and explicit approximate solutions, Journal of the Electrochemical Society 146 (1999) 4183–4188.
[31] R.D. Shannon, Revised effective ionic radii and systematic studies of inter atomic distances in halide and chalcogenides, Acta Crystallographica A 32 (1976) 751–767.
[32] H.L. Tuller, Ionic conduction in nanocrystalline materials, Solid State Ionics 131 (2000) 143–157.
[33] X. Guo, Z. Zhang, Grain size dependent grain boundary defect structure: case of doped zirconia, Acta Materialia 51 (2003) 2539–2547.
[34] H. Li, C. Xia, M. Zhu, Z. Zhou, G. Meng, Reactive $Ce_{0.8}Sm_{0.2}O_{1.9}$ powder synthesized by carbonate coprecipitation: sintering and electrical characteristics, Acta Materialia 54 (2006) 721–727.